



AstroX/McXtrace 2021

An update on simulation examples and features

Knudsen, Erik B.; Jegers, Arne S.; Beck, Jens H.; Ferriera, D. M.

Published in:
Proceedings of SPIE

Link to article, DOI:
[10.1117/12.2594555](https://doi.org/10.1117/12.2594555)

Publication date:
2021

Document Version
Publisher's PDF, also known as Version of record

[Link back to DTU Orbit](#)

Citation (APA):
Knudsen, E. B., Jegers, A. S., Beck, J. H., & Ferriera, D. M. (2021). AstroX/McXtrace 2021: An update on simulation examples and features. In S. L. O'Dell, J. A. Gaskin, & G. Pareschi (Eds.), *Proceedings of SPIE: Optics for EUV, X-Ray, and Gamma-Ray Astronomy X* Article 118220Q SPIE - International Society for Optical Engineering. <https://doi.org/10.1117/12.2594555>

General rights

Copyright and moral rights for the publications made accessible in the public portal are retained by the authors and/or other copyright owners and it is a condition of accessing publications that users recognise and abide by the legal requirements associated with these rights.

- Users may download and print one copy of any publication from the public portal for the purpose of private study or research.
- You may not further distribute the material or use it for any profit-making activity or commercial gain
- You may freely distribute the URL identifying the publication in the public portal

If you believe that this document breaches copyright please contact us providing details, and we will remove access to the work immediately and investigate your claim.

AstroX/McXtrace 2021 - an update on simulation examples and features.

Erik B. Knudsen^a, Arne S Jegers^b, Jens H. Beck^b, and Desiree D. M. Ferreira^b

^aDTU Physics, Fysikvej, building 307, DK-2800 Kgs. Lyngby, Denmark

^bDTU Space, Elektrovej, building 327, DK-2800 Kgs. Lyngby, Denmark

ABSTRACT

AstroX is an add-on toolbox to the open source X-ray simulation software package McXtrace, which introduces Astronomical telescope optics and features to the package. Thus, enabling users to draw from the experience and developments of two communities. It may also shed further light into calibration results when measuring optics in ground based test-setups, at synchrotrons and specialized facilities.

AstroX now includes a range of optical elements for Wolter class optics, extended source models, lobster eye optics, and gratings etc. Furthermore the open modular nature of McXtrace makes it fairly simple to connect to other software packages.

We present a range of simulations of various aspects of telescopes:

- A simulation workflow capable of quantifying stray light from Compton scattering at mirror substrates.
- A study on the effect of dust contamination inside small-pore silicon pore optics.
- A mechanism to include gratings for spectrometry in a telescope simulation.

Keywords: Ray tracing, X-ray, simulation, McXtrace, telescope, AstroX

1. INTRODUCTION

The performance of X-ray telescopes are often regarded as simply the response of its mirrors. In many cases also the collective effect of mirror reflectivity with imperfections to the mirrors (figure errors, slope errors, roughness, misalignment etc.) is included in the analysis. Such effects are often studied within the geometrical optics paradigm, mainly for the reason that ray tracing is a fairly simple process to program and is often fast in terms of computer run time. The AstroX toolbox adds to the McXtrace package and builds on the idea that a versatile framework can be used to simulate multiple types of telescopes as opposed to rebuilding a new ray-tracing engine for each new mission. The toolbox itself continues to develop, and in the following we will present some novel use-cases and supporting calculations.

This article addresses three topics in relation to computation of Wolter-class telescope optics in general: First, in recent years, Silicon Pore Optics (SPOs) have been proposed as a technical solution to produce lightweight, large scale Wolter class telescopes.¹ A downside to this is that material is placed in the optical field, which could create spurious signals. Thus, a tool to evaluate and quantify such signals becomes important. We present a workflow that adds up to such a tool applied to the Chandra X-ray Observatory (CXO).

Second, a further characteristic of SPOs is that the transmission channels by design are relatively small. This creates a confined space, in which dust particles may be trapped at assembly. The second track of this article concerns itself with the effect of absorption caused by dust particles.

Third, many missions/telescopes include devices for wavelength separation. One of the most common schemes is to include have a grating disperse energies spatially.^{2,3} We present a way of including these kinds of devices in the frame of AstroX/McXtrace as applied to CXO.

Further author information: (Send correspondence to E.B.K.)

E.B.K.: E-mail: erkn@fysik.dtu.dk, Telephone: +45 4525 3344

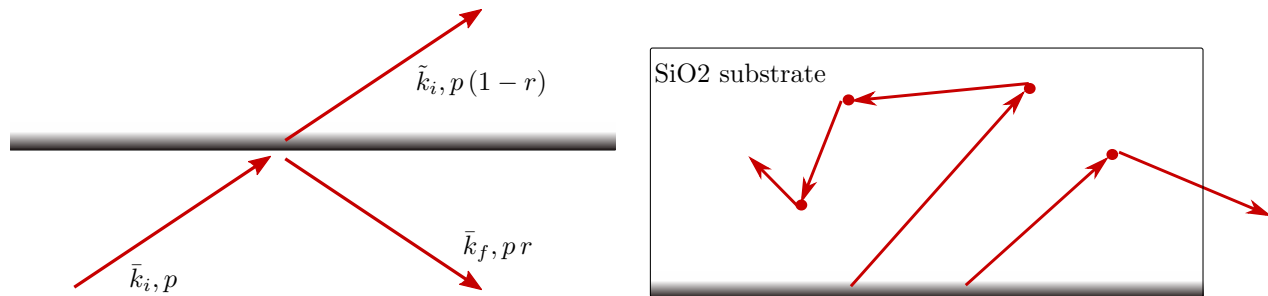


Figure 1. Left: Schematic drawing of the process applied when storing pseudo-photons at reflection points. A Monte Carlo photon with wavevector \bar{k}_i , arrives at the mirror surface and gets reflected into \bar{k}_f . Its Monte Carlo weight p is adjusted according to the reflectivity r of the mirror surface. The "removed" weight $p(1-r)$ is then attached to a pseudo photon travelling in the original direction $\bar{k}_i \parallel \bar{k}_i$, i.e. into the surface.

Right: Drawing of two Monte Carlo pseudo photons that have entered a mirror SiO₂ substrate and scatter (Compton) inside. Scatter events are indicated by the red dots. For Compton-scattering the photons lose energy at each interaction. This effect is encoded in the shorter wavevector k .

2. METHOD

2.1 Substrate Compton scattering

From a particle perspective, a photon impinging on a surface may be either reflected or transmitted into the surface. In the context of Monte Carlo (MC) ray tracing this is often associated with a re-weighting of the MC photon, to retain statistical significance in the signal path.⁴ If, instead the transmission branch is of interested we may simply take the complementary weight $T = (1 - R)$ and allow the photon to enter the mirror substrate.

We apply a concept of logging reflections, in terms of the photon state before and after, in a preset region.⁵ At the points of reflection a MC photon, dubbed pseudo-photon to distinguish it from the regular MC photons, is emitted representing the non-reflected portion of the beam. Each pseudo photon is traced into the mirror substrates and allowed to interact with material therein, for instance by means of Compton-scattering.⁶ Although the likelihood is small, scattered photons may scatter multiple times within the substrate, but also between mirror substrates. Each time a scattering event occurs, that event is yet again logged. Thus we may create scattering maps which may be analyzed to determine what objects generate (unwanted) spurious signal pathways to the detector, and hence contribute to the overall noise level of measurements. To summarize the process:

1. Use a **Scatter_logger**-instance in a AstroX/McXtrace-model of CXO to compute the intensity field that enter the mirror SiO₂-substrates.
2. run a 2nd instance of the AstroX/McXtrace model of CXO which contains the mirror substrates defined by means of **Union**⁷-building blocks and a Compton scattering process enabled.
3. Store scattering points and trace the scattered photons until they terminate outside the telescope or hit the detector.

2.2 Dust contamination

As a first order approximation to the dust particle contamination problem, we consider dust particles to be opaque, i.e. to have infinite absorption regardless of photon energy. This obviously forms also an upper bound on the absorption effect of dust particles. A simple extension to this theory is impose a chemical composition of the dust particles, and hence by means of Beer-Lambert's law⁸ apply a transmission coefficient.

To determine the effect of dust particles, we assume that the particles are randomly scattered and oriented in the pore. It follows from the random orientation that the shape of dust particles may be approximated by perfect spheres, from which it in turn follows that the cross section of a particle become a circle. We write the dust particle cross section, A_p , as:

$$A_p = \pi \cdot \left(\frac{D}{2}\right)^2 \quad (1)$$

Table 1. Number of allowed particles above a given size (diameter) in a m³ for a few clean room ISO classes, and US-standard equivalents.⁹ ISO class 9 constitutes room air.

CLASS	FED209E	> 0.1 μm	> 0.2 μm	> 0.3 μm	> 0.5 μm	> 1 μm	> 5 μm
ISO 1		10	2				
ISO 5	100	100000	23700	10200	3520	832	29
ISO 9					35200000	8320000	293000

Where D is the diameter of the particle. When a photon travels a small distance through a pore (dl) the probability that it will hit a dust particle is equal to the number of particles in the volume it has passed times how much of the area a particle fills:

$$dP = w h dl \rho_p(D) \frac{A_p}{w h} = A_p \rho_p(D) dl = \pi \left(\frac{D}{2} \right)^2 \rho_p(D) dl = \frac{\pi}{4} D^2 \rho_p(D) dl \quad (2)$$

where w, h are the width and height of the pore, ρ_p is the concentration of particles for a given diameter, and A_p the cross section area of the particle. Here we have approximated the pores in a Wolter optics by square straight channels.

According to the ISO standard for cleanrooms⁹ particle concentrations may be calculated using the following formula

$$\rho_p(D) = 10^N \left(\frac{0.1}{D} \right)^{2.08} \quad (3)$$

To exemplify, we have reproduced particle concentrations for a standard set of particles in a few ISO cleanroom classes in table 1. Using the discrete values for particle size we may write the total probability for collision with a dust particle as:

$$dP = \frac{\pi}{4} \left(\sum D^2 \rho_p(D) \right) dl \quad (4)$$

If dust particles are considered opaque (completely absorbing) the pre-factor to dl in eq. (4) may be identified with the linear absorption factor in Beer-Lambert's law (eq. (5)).

$$\frac{I}{I_0} = \exp(-\mu l) \quad (5)$$

Although opaque particles form a useful upper bound for the absorption effect, it is clear that the material composition of dust particles may have a significant impact on the attenuation, in the sense that some fraction of radiation will pass through. To account for such partially transparent dust particles, we may again apply eq. (5) on a single particle level, using an appropriate linear absorption coefficient for the composition, μ_{mat} , and the mean length, l_m travelled through a dust particle. The mean length through a sphere is simply the ratio of the sphere's volume to the cross section area of the sphere.

$$l_m = \frac{\frac{4}{3} \pi r^3}{\pi r^2} = \frac{4r}{3} = \frac{2D}{3} \quad (6)$$

Finally, the pores in an SPO are generally not square and straight, instead they follow a curved profile, e.g. in a true Wolter-I¹⁰ context each pore consists of a parabolic/hyperbolic pair. Within the AstroX/McXtrace system, the time elapsed when a ray travels is tracked by default. Hence, we may easily implement absorption due to dust-particles in the Monte Carlo scheme by simply applying Beer-Lambert's law to the photon weight, post traversal of pores.

$$\frac{p}{p_0} = \exp\left(-\mu \frac{t - t_0}{c}\right) \quad (7)$$

2.3 Gratings

The CXO has a grating module installed to allow energy-dispersed observations. In fact the telescope has as two sets, but for brevity we shall limit our discussion to the High Energy Transmission Grating (HETG).¹¹ The HETG-module may be swung into the optical path on request. The module consists of a large set of grating tiles that cover the four circular mirror exits. The two inner mirrors, which in general reflect more of high energy radiation due to their relatively smaller incidence angles, are covered by a set of High Energy Gratings (HEG), whereas the outer rings are covered by Medium Energy Gratings (MEG). The grating parameters are given in Ref. 11, some of which are reproduced here in table 2. Although any grating detector combination is possible, the gratings on CXO are optimized for use with the ACIS-S detector module, which consists of 6 tiles of 2D pixel area detectors set in a horizontal line.¹²

For ray tracing a transmission grating it is necessary to conceptually consider the ray a plane wave at the moment of diffraction within the grating model. In practice, within the domain of MC ray tracing, this simply amounts to computing a probability distribution function from which to sample outgoing angles. To exemplify we may pick a diffraction order from available diffraction orders with the relative probabilities (following Ref. 13):

$$P(N) = \frac{p_0(N)}{\sum_{n=N} p_0(n)} \quad (8)$$

where:

$$p_0(n) = \begin{cases} \left(\frac{\sin(\gamma n \pi)}{n \pi} \right)^2 (1 + e^{-2kz_d \beta} - 2e^{-kz_d \beta} \cos(kz_d \delta)); & n \neq 0 \\ \gamma^2 + (1 - \gamma)^2 e^{-2kz_d \beta} - 2\gamma(1 - \gamma)e^{-kz_d \beta} \cos(kz_d \delta); & n = 0 \end{cases} \quad (9)$$

Here z_d is the thickness of grating rods, δ and β the real and imaginary parts of the refractive index differences from unity: $n = 1 + \delta + i\beta$, and γ the duty cycle of the grating. Given the relative order probabilities, we may readily pick an outgoing angle by first picking an order by a Monte Carlo choice, and subsequently pick an angle centred on the angle given by eq. (10).

$$\theta_0(n) = \frac{n2\pi}{k\Lambda} \quad (10)$$

Here Λ denotes the the grating period. Figure 2 shows the computed grating diffraction patterns for HEG and MEG, when illuminated by 1keV radiation. We may note the difference in relative intensity for 2nd order diffraction for the two gratings, which is caused by the difference in duty cycle. In CXO, in order to easily separate the signals from the two grating types, the gratings are mounted at angles as indicated in table 2. The upshot of this is that the energy resolved signal will form an elongated X on the detector array.

3. RESULTS

3.1 Compton substrate scattering

In the following we illuminated by X-ray radiation drawn from a uniform spectrum in the energy range: $E = 0.1$ to 100keV. Figure 3 shows spatially resolved maps of the intensity scattered inside the CXO optics, where scattered intensity is binned according to its point of origin inside the mirror substrates. It is clear from fig. 3 that the biggest contribution to substrate scattering comes from the secondary mirror. This may be explained by the larger incidence angles experienced here.

Table 2. Main grating parameters - the ones used in simulations in section 3. From Ref. 11.

	MEG	HEG
line density /mm	2000	4000
material	Au	Au
duty cycle	0.4	0.3
tilt angle / °	4.725	-5.235
size / mm ²	25 x 25	25 x 25

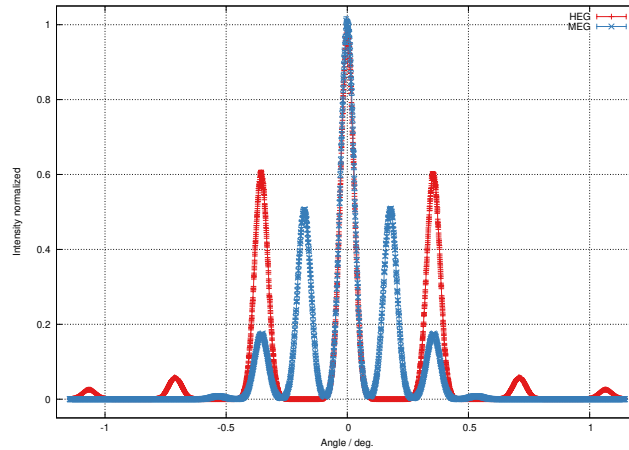


Figure 2. Example grating diffraction patterns for the HEG and MEG Au-gratings with 4000 and 2000 lines / mm, resp. (Parameters given in table 2) when illuminated by 1keV radiation.

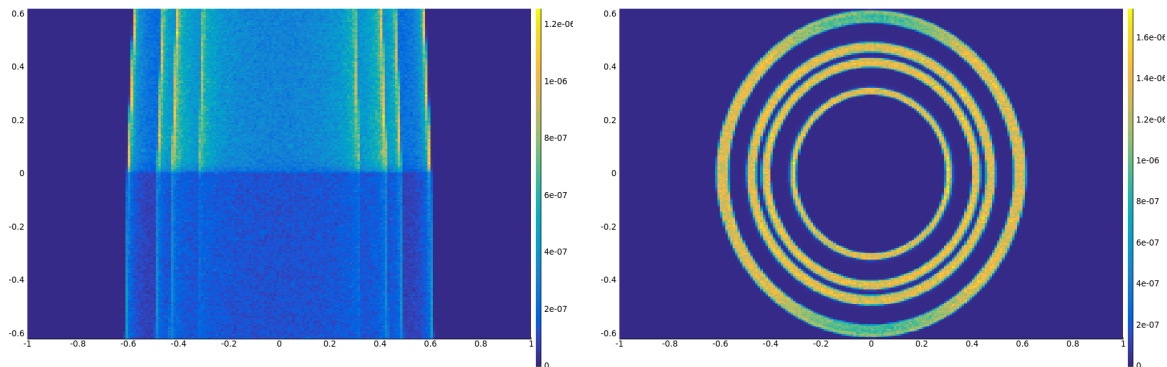


Figure 3. Spatially resolved maps of mirror substrate Compton scattering locations in the CXO telescope optic. Left: XZ-projection; right: XY-projection.

In fig. 4 we show the resulting radiation pattern, that is the result of unreflected intensity in the telescope. Unsurprisingly, most of the intensity that enters into the mirror substrates passes through (The central high-intensity region in fig. 4 left.). The Compton-scattered part of the radiation is the diffuse background we find in a wide angular range around the centre. The right hand side of fig. 4 shows the signal caught on the ACIS-I imaging modules 0 to 3. As expected, we find no significant difference between the modules. We may conclude that, although the available Monte Carlo statistics are very limited, the Compton scattering originating from the mirror substrates, is unlikely to significantly degrade the telescope signal.

3.2 Dust Contamination

For this section we have used a version the proposed ATHENA optic as described in Refs. 14,15 as a starting point. Note that this is not the final design, nonetheless the result should be valid for similar SPO structures. According to plan^{14,15} the optics is to be constructed with pores of $1 \times 0.7\text{mm}^2$ in the length range 0.2 to 0.4m.

The particle concentration may be found from the clean room classification, reproduced for reference in table 1

In the following we will refine our analysis by assuming that dust is composed of Si and/or C and look up absorption coefficients accordingly. In the ATHENA case the SPO modules are (to be) assembled in a ISO 5 class (class 100) cleanroom. With input from table 1, and following eqs. (5) and (6) we may compute the total absorption as a function of composition and wavelength. Figure 5 shows the attenuation coefficient associated with free floating dust particles in an SPO-optic assembled in a class ISO 5 room. In the ATHENA context, the

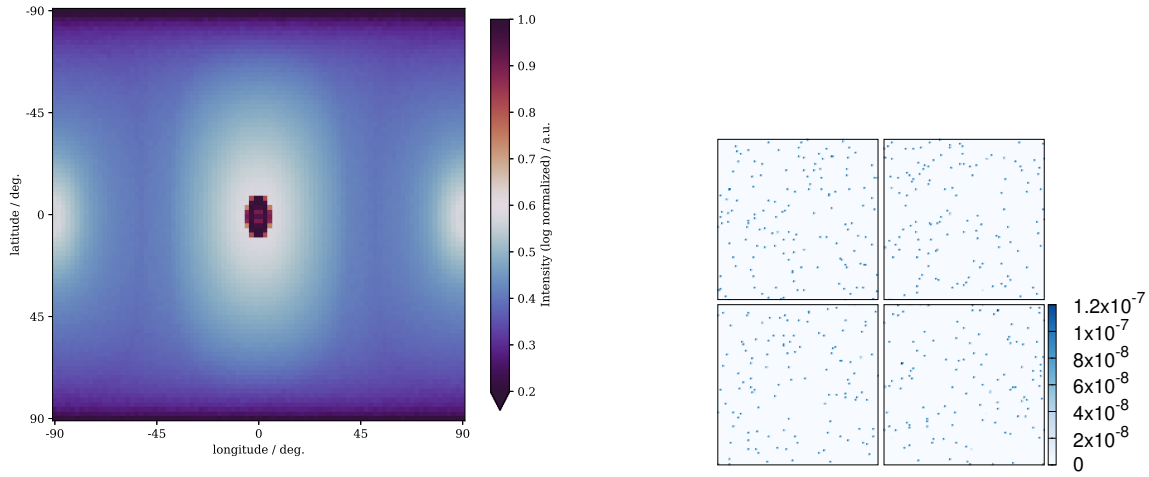


Figure 4. Compton scattering from the mirror substrates of CXO. Left: Intensity caught on a spherical surface completely surrounding the telescope optic. The high intensity circular area around (long., lat.) = (0, 0)° corresponds to unscattered intensity through the substrates. Right: Scattered signal that reaches the 4 imaging detector modules ACIS_I0 to 3.

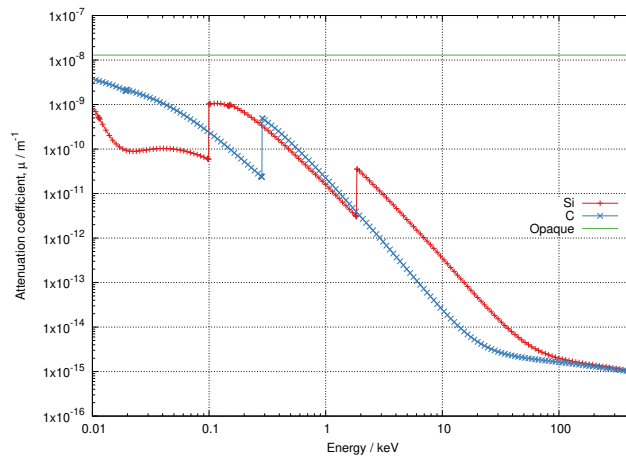


Figure 5. Linear attenuation coefficients associated with free floating dust particles inside pores of an SPO assembled under clean room ISO class 5 conditions. Dust is considered dilute spheres, uniformly distributed throughout the pore. Blue: Si-dust particles; Red: C-dust particles; Green: opaque dust particles.

upper bound formed by opaque particles (eq. (4)) indicate a total attenuation caused by free dust of:

$$\frac{I}{I_0} < \exp(1.3 \times 10^{-8} \cdot 0.203) \approx 1 - 2.6 \times 10^{-9} \quad (11)$$

for the set of longest pores ($L \approx 2 \times 0.1015\text{m}$, in the inner ring) in the considered ATHENA optic version. Thus, the clear prediction is that free floating dust absorption is far from significant, for this level of clean air.

Using the time tracking feature of McXtrace/AstroX (section 2) we can directly apply dust-absorption corrections in a telescope model. Since it is a very minor effect, for clarity we choose to visualize the effective pore-length experienced by the transmitted radiation. Figure 6 and table 3 show distributions of ray path lengths through a set of pores at rings 1, 7, and 15 of the ATHENA-optic version under consideration here. We stress that this is a preliminary version of the optic which is subject to change as the project matures towards

Table 3. Mean and standard deviation of the pore path length experienced by rays passing through pores in rings 1, 7, and 15 of the considered ATHENA optics version.

ring #	mean / m	std. dev. / m
1	0.203	4.95×10^{-6}
7	0.0882	9.66×10^{-6}
15	0.0504	2.36×10^{-5}

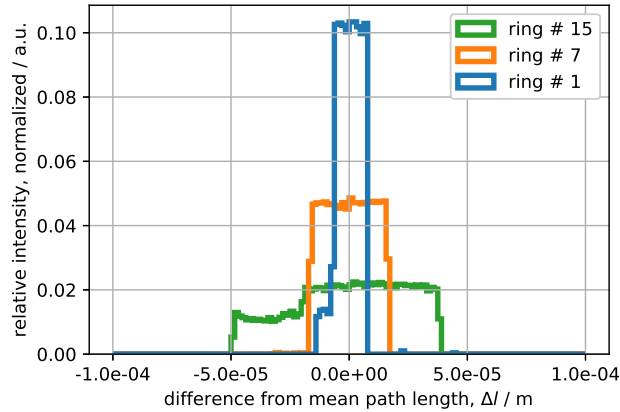


Figure 6. Effective pore-length for a few rings in the proposed ATHENA-optic.¹⁵

realization. From the effective path length we find correction factor to eq. (11) of

$$\delta l = \pm 4.95 \times 10^{-6} \text{ m} \Rightarrow \delta \left(\frac{I}{I_0} \right) = \pm 0.4 \times 10^{-11} \quad (12)$$

3.3 Gratings

We have added into our model of CXO optional gratings with parameters from table 2. These are placed in relation to the nominal focal point, placed 8.632 m upstream from the aimpoint on a line towards the mid-plane radii of the 4 mirrors. Further, (as noted in section 2 the outer MEGs have been tilted by 4.725° and the inner HEGs by -5.235° around the optical axis. In the focal plane we have placed 5 2D-monitors in a horizontal line with gaps mimicking those in the in-flight telescope. To avoid the clutter of 192 and 144 individual gratings in the model, we have simplified the geometry to only a single grating per mirror, and restricted the radiation to only illuminate the portion of the mirror that reflects to the gratings (fig. 7).

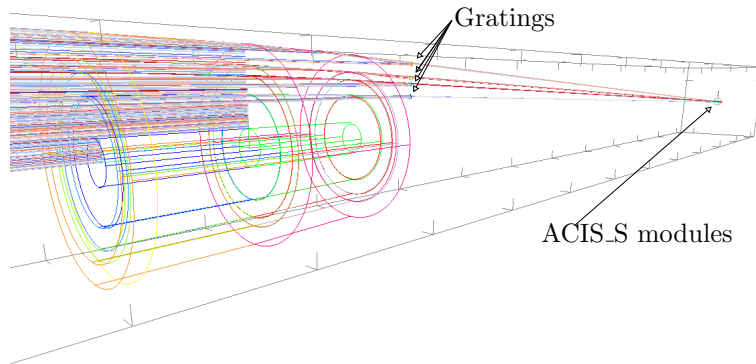


Figure 7. visual ray tracing of the cxo-model. the set of single gratings are labelled.

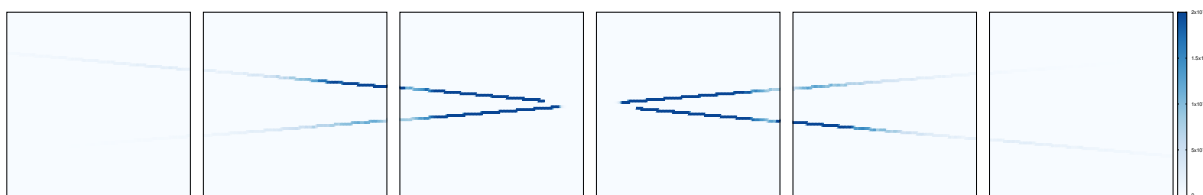


Figure 8. Raw detector images from the McXtrace/AstroX CXO-model, where the detector modules mimic the ACIS-S setup. Gratings and optic are illuminated by a mathematical point source which radiates towards the sector of the optics which reflects onto the gratings. The source emits X-ray uniformly in the energy interval 0.6 keV to 9.4 keV. From left to right ACIS-S modules 0 to 5.

Figure 8 shows the set of ACIS-S modules seen by the simulated CXO-model when the gratings are illuminated as discussed above with a source emitting X-rays in a uniform energy distribution between 0.6 and 9.4 keV. As expected, the intensity is dispersed in an elongated X-shape, and from this we conclude that the model works as intended. For simplicity we have in the model system, neglected the offset of the focal point. In reality the telescope focal point is situated slightly inside ACIS-S 3.¹² To include the offset is a straightforward translation of the set of detector modules.

4. CONCLUSION/SUMMARY

We may draw a couple of conclusions in terms of numerical results: First, we find that in terms of dust contamination, free flowing dust in a clean room will not impair the performance of an SPO based telescope - In fact even if the optic was assembled in room air, this would still be expected to be the case. Second, we find likewise, that Compton scattering from glass mirror substrates is not likely to be impair telescope performance.

More importantly, we have shown three workflows providing handles on very different aspects of telescope performance using the AstroX/McXtrace framework. These are use-cases that are not limited to the examples we have shown here, and in all three cases may be expanded upon at will. Note, that the code used will be publicly available under an open source license.

ACKNOWLEDGMENTS

This work has been supported by the European Space Agency under contract 4000114410/15/NL/BW. The authors acknowledge M. Bertelsen, and E.B. Klinkby for scientific discussions.

REFERENCES

- [1] Collon, M. J., Günther, R., Kraft, S., Beijersbergen, M. W., Bavdaz, M., Wallace, K., Krumrey, M., and Freyberg, M., "Silicon pore optics for astrophysical x-ray missions," in [*Optics for EUV, X-Ray, and Gamma-Ray Astronomy III*], **6688**, 668813, SPIE (9 2007).
- [2] Speybroeck, L. V., "Spectroscopic Techniques in X-Ray Astronomy," *International Astronomical Union Colloquium* **14**, 845–869 (11 1972).
- [3] Gursky, H. and Zehnpfennig, T., "An Image-Forming Slitless Spectrometer for Soft X-Ray Astronomy," *Applied Optics* **5**(5), 875–876 (1966).
- [4] James, F., "Monte Carlo theory and practice," *Reports on Progress in Physics* **1145** (1980).
- [5] Bergbäck Knudsen, E., Bryndt Klinkby, E., and Kjær Willendrup, P., "McStas event logger: Definition and applications," *Nuclear Instruments and Methods in Physics Research, Section A: Accelerators, Spectrometers, Detectors and Associated Equipment* **738**, 20–24 (2014).
- [6] Cheston, W. B., "Compton Scattering," *Physical Review* **95**(1), 247–248 (1954).
- [7] Bertelsen, M., "Software for simulation and design of neutron scattering instrumentation," (2017).
- [8] Ingle Jr, J. D. and Crouch, S. R., [*Spectrochemical analysis*] (1988).

- [9] European Committee for Standardization, “INTERNATIONAL STANDARD ISO 14644-1,” tech. rep., ISO (2015).
- [10] Wolter, H., “Spiegelsysteme streifenden Einfalls als abbildende Optiken für Röntgenstrahlen,” *Annalen der Physik* **10**(1-2), 94–114 (1952).
- [11] Canizares, C. R., Davis, J. E., Dewey, D., Flanagan, K. A., Galton, E. B., Huenemoerder, D. P., Ishibashi, K., Markert, T. H., Marshall, H. L., Mcguirk, M., Schattenburg, M. L., Schulz, N. S., Smith, H. I., and Wise, M., “The Chandra High-Energy Transmission Grating: Design, Fabrication, Ground Calibration, and 5 Years in Flight,” *Publications of the Astronomical Society of the Pacific* **117**, 1144–1171 (2005).
- [12] “The Chandra Proposers’ Observatory Guide,” (2019).
- [13] Schnopper, H. W., Van Speybroeck, L. P., Delvaille, J. P., Epstein, A., Killne, E., Bachrach, R. Z., Dijkstra, J., and Lantward, L., “Diffraction grating transmission efficiencies for XUV and soft x rays,” *Applied Optics* **16**(4), 1088–1091 (1977).
- [14] Willingale, R., Pareschi, G., Christensen, F., and den Herder, J.-W., “The hot and energetic universe: The optical design of the athena+ mirror,” (2013).
- [15] Nandra, K., Barret, D., Barcons, X., Fabian, A., den Herder, J.-W., Piro, L., Watson, M., Adami, C., Aird, J., Afonso, J. M., Alexander, D., Argiroffi, C., Amati, L., Arnaud, M., Atteia, J.-L., Audard, M., Badenes, C., Ballet, J., Ballo, L., Bamba, A., Bhardwaj, A., Battistelli, E. S., Becker, W., Becker, M. D., Behar, E., Bianchi, S., Biffi, V., Birzan, L., Bocchino, F., Bogdanov, S., Boirin, L., Boller, T., Borgani, S., Borm, K., Bouché, N., Bourdin, H., Bower, R., Braitto, V., Branchini, E., Branduardi-Raymont, G., Bregman, J., Brenneman, L., Brightman, M., Brüggen, M., Buchner, J., Bulbul, E., Brusa, M., Bursa, M., Caccianiga, A., Cackett, E., Campana, S., Cappelluti, N., Cappi, M., Carrera, F., Ceballos, M., Christensen, F., Chu, Y.-H., Churazov, E., Clerc, N., Corbel, S., Corral, A., Comastri, A., Costantini, E., Croston, J., Dadina, M., D’Ai, A., Decourchelle, A., Ceca, R. D., Dennerl, K., Dolag, K., Done, C., Dovciak, M., Drake, J., Eckert, D., Edge, A., Etori, S., Ezoe, Y., Feigelson, E., Fender, R., Feruglio, C., Finoguenov, A., Fiore, F., Galeazzi, M., Gallagher, S., Gandhi, P., Gaspari, M., Gastaldello, F., Georgakakis, A., Georgantopoulos, I., Gilfanov, M., Gitti, M., Gladstone, R., Goosmann, R., Gosset, E., Grosso, N., Guedel, M., Guerrero, M., Haberl, F., Hardcastle, M., Heinz, S., Herrero, A. A., Hervé, A., Holmstrom, M., Iwasawa, K., Jonker, P., Kaastra, J., Kara, E., Karas, V., Kastner, J., King, A., Kosenko, D., Koutroumpa, D., Kraft, R., Kreykenbohm, I., Lallement, R., Lanzuisi, G., Lee, J., Lemoine-Goumard, M., Lobban, A., Lodato, G., Lovisari, L., Lotti, S., McCharthy, I., McNamara, B., Maggio, A., Maiolino, R., Marco, B. D., de Martino, D., Mateos, S., Matt, G., Maughan, B., Mazzotta, P., Mendez, M., Merloni, A., Micela, G., Miceli, M., Mignani, R., Miller, J., Miniutti, G., Molendi, S., Montez, R., Moretti, A., Motch, C., Nazé, Y., Nevalainen, J., Nicastro, F., Nulsen, P., Ohashi, T., O’Brien, P., Osborne, J., Oskinova, L., Pacaud, F., Paerels, F., Page, M., Papadakis, I., Pareschi, G., Petre, R., Petrucci, P.-O., Piconcelli, E., Pillitteri, I., Pinto, C., de Plaa, J., Pointecouteau, E., Ponman, T., Ponti, G., Porquet, D., Pounds, K., Pratt, G., Predehl, P., Proga, D., Psaltis, D., Rafferty, D., Ramos-Ceja, M., Ranalli, P., Rasia, E., Rau, A., Rauw, G., Rea, N., Read, A., Reeves, J., Reiprich, T., Renaud, M., Reynolds, C., Risaliti, G., Rodriguez, J., Hidalgo, P. R., Roncarelli, M., Rosario, D., Rossetti, M., Rozanska, A., Rovilos, E., Salvaterra, R., Salvato, M., Salvo, T. D., Sanders, J., Sanz-Forcada, J., Schawinski, K., Schaye, J., Schwöpe, A., Sciortino, S., Severgnini, P., Shankar, F., Sijacki, D., Sim, S., Schmid, C., Smith, R., Steiner, A., Stelzer, B., Stewart, G., Strohmayer, T., Strüder, L., Sun, M., Takei, Y., Tatischeff, V., Tiengo, A., Tombesi, F., Trinchieri, G., Tsuru, T. G., Ud-Doula, A., Ursino, E., Valencic, L., Vanzella, E., Vaughan, S., Vignali, C., Vink, J., Vito, F., Volonteri, M., Wang, D., Webb, N., Willingale, R., Wilms, J., Wise, M., Worrall, D., Young, A., Zampieri, L., Zand, J. I., Zane, S., Zezas, A., Zhang, Y., and Zhuravleva, I., “The hot and energetic universe: A white paper presenting the science theme motivating the athena+ mission,” (2013).